Journal of Fluids and Structures 87 (2019) 102–123

Contents lists available at ScienceDirect

Journal of Fluids and Structures

journal homepage: www.elsevier.com/locate/jfs

On the influence of the free surface on a stationary circular cylinder with a flexible splitter plate in laminar regime

H.R. Díaz-Ojeda [a,*], L.M. González [a], F.J. Huera-Huarte [b]

[a] CEHINAV, ETSIN, Universidad Politécnica de Madrid (UPM), Arco de la Victoria 4, 28040 Madrid, Spain
[b] Department of Mechanical Engineering, Universitat Rovira i Virgili., 43007 Tarragona, Spain

HIGHLIGHTS

- A 2D analysis of the dynamics of a flexible splitter plate attached to the base of a cylinder, in laminar regime has been carried out, using numerical techniques.
- Simulations are validated using a benchmark exercise as in Turek et al. (2010).
- The amplitude of the oscillations of the splitter plate increases with Reynolds, Froude and Cauchy numbers as well as with depth.
- Drag coefficient increases linearly with depth, and decreases with decreasing fluid viscosity.

ARTICLE INFO

Article history:
Received 2 November 2018
Received in revised form 5 March 2019
Accepted 12 March 2019
Available online 29 March 2019

Keywords:
Fluid–Structure Interaction (FSI)
Free-surface
Flexible splitter plate
Stationary cylinder
OpenFoam-extend

ABSTRACT

Fluid Structure Interaction (FSI) problems typically found in offshore systems and other oceanic applications are generically affected by the proximity to the free surface. The aim of this paper is to evaluate to what extent the immersion depth affects the dynamics of a simplified fluid–structure interaction model. We have selected the research conducted by Turek et al. (2010), in which a deformable splitter plate is attached to the base of a stationary circular cylinder, and a uniform flow is imposed to the system, in laminar regime. We validate our numerical techniques by reproducing the results obtained by other authors when simulating this problem, as in a benchmark exercise.

After the initial validation, the structure is submerged on a liquid phase that is separated by a free surface from the gas phase placed on the top. The structure is submerged at different depths and the dependence on the Cauchy, Reynolds and Froude numbers are studied. The deformation and the drag forces acting on the structure are analysed in detail in order to understand the effects that the free surface has on the problem. It was observed that the amplitude of the tip of the splitter plate grows as the Reynolds, Froude and Cauchy numbers are increased. However, as the depth is increased, and the structure moves away from the interface, all measurements tend to saturate. For lower depths, the free surface works as a damper for the plate dynamics, reducing the oscillations. The physical mechanism of deformation based on the pressure difference at both sides of the plate is studied, monitoring how the pressure difference decreases as the structure approaches the free surface. The drag coefficient of the global structure (cylinder and plate) increases linearly with depth, but decreases when the viscosity of the fluid is reduced.

* Corresponding author.
E-mail address: hector.diaz@upm.es (H.R. Díaz-Ojeda).

https://doi.org/10.1016/j.jfluidstructs.2019.03.009
0889-9746/

1. Introduction

The analysis of Fluid–Structure Interactions (FSI) with large-scale flow-induced structural deformations, is crucial in applications that range from complex biomedical flows to other classical engineering systems. Future energy projects tend towards to the sea as one of the most important energy resources for future applications, and a wide variety of energy-harvesting devices are now being developed, to extract energy from ocean waves and sea currents. In the ocean environment, systems are forced to interact with the sea dynamics and consequently are deformed by sea loads. Unexpected failures can have catastrophic economical implications since budgets tend to be very large. Generally, submerged elastic structures are being constantly deformed by the sea currents near water's surface. When the motion of such submerged objects is equal to one of the natural frequencies, the fatigue life decreases rapidly. Today, empirical methods are the leading approach for simulating these phenomena, but numerical methods based on FSI become more and more attractive, as computational capabilities are constantly improving. Researchers have recently focused on mechanisms such as the utilization of a flexible splitter plate not only for modulation of vortex shedding or flow-induced vibration suppression (Assi et al., 2009; Huera-Huarte, 2014), but also for energy harvesting. Taylor et al. (2001), Allen and Smits (2001) examined the feasibility of a flexible splitter plate, which is made of a piezoelectric membrane attached to a bluff body for electricity generation from vortex-shedding-induced vibration of the plate.

From the research perspective, the interaction of shear flows with the ocean's surface is a challenging fluid mechanic problems. The flow around submerged objects imply fully three dimensional complex vortical structures which interact with the free surface. The vortex shedding behind a bluff body causes unsteady pressure drops on the rear surface of the body leading to drag and lift fluctuations. The vibration magnitude of a splitter plate attached to a bluff body in its wake region, can be characterized by the unsteady pressure loading due to vortex shedding in the wake region, and by the flexibility of the plate. Due to its practical importance in many engineering problems, much attention has been devoted to manipulating vortex shedding with active and/or passive means. Among them, attaching a splitter plate to the cylinder base has been known to be one of the most successful ways to control vortex shedding (Lou et al., 2016). As the shape of both submerged objects and the free surface deform in time, the flow field around the object also changes. In those situations where the deformations of the object are large and strongly affect the flow field, the fluid and the solid equations are fully coupled, and consequently a two-way FSI must be implemented.

As numerical methods play an important role in predicting hydrodynamic motion and forces on these submerged objects, an FSI benchmark for flow-induced deformation of thin elastic structures is necessary. The study of the self-sustained oscillation of an elastic splitter plate attached to the lee side of a rigid cylinder in two-dimensional laminar channel flows (Turek et al., 2010) is currently considered a standard benchmark for FSI. Previous studies documented the effects of the material properties of the structure and flow conditions on the response of the structure. In the absence of free surface, the behaviour of the plate is a function of the vortex-shedding frequency and the natural frequency of the plate. The vortex shedding frequency is determined by the shape of the body and the Reynolds number, while the natural frequency of the plate is determined by Young's modulus and its geometric parameters, especially the length of the plate. Despite increasing engineering interest, Lee and You (2013) stated that the quantitative relationship between the characteristics of the vortices shed, the material and geometric properties of the plate that describe the influence on the drag and lift acting on the bluff body and the vibration of the plate, are not well understood even without free surface. In Bhardwaj and Mittal (2012) the effect of Reynolds number, material properties and geometric non-linearity on the plate displacement as well as its frequency in the FSI benchmark proposed by Turek et al. (2010) was quantified. They showed that the oscillation frequency of the plate varies linearly with dilatational wave speed inside the plate (or its natural oscillation frequencies). The plate length influences vibration modes of the splitter plate, and the plate displacement is a function of Young's Modulus and its natural frequencies, see Lee and You (2013). An experimental study found that the plate displacement collapses on a single curve for different cases of dimensionless bending stiffness (Shukla et al., 2013). It is also well known that the oscillation amplitude and frequency of the plate tip is strongly affected by the combined effects of blockage and cylinder size (Gallegos and Sharma, 2016).

A second perspective, which also points out the importance of the FSI problems involving free surface deformation, comes to us from the traces left on the ocean by viscous wakes, and detected by radar observations of the ocean surface. There is no complete theoretical explanation of such traces owing to the great complexity of the problem. The linear problem of two-dimensional shear-flow/surface interaction was investigated by Triantafyllou and Dimas (1989), who found that two distinct regimes of unstable waves exist depending on the Froude and wavenumber. In Dimas and Triantafyllou (1994), the nonlinear evolution of the two branches of unstable waves are studied assuming an inviscid flow due to the high Reynolds numbers.

Simplified approaches, such as the two-dimensional flow past a cylinder close to a free surface, have been numerically investigated by Reichl et al. (2005) and Bouscasse et al. (2017). The wake behaviour at a Reynolds number of 180, for Froude numbers between 0.0 and 0.7, and for gap ratios between 0.1 and 5.0 was examined. Different free surface deformations can be observed according to the Froude numbers used. This is associated with supercritical to subcritical transitions in the near wake resulting in localized free-surface sharpening and wave breaking. Since surface vorticity is directly related to surface curvature, such high surface deformation results in significant surface vorticity, which can diffuse and then convect into the main flow, altering the development of Strouhal vortices from the top shear layer and affecting wake skewness.

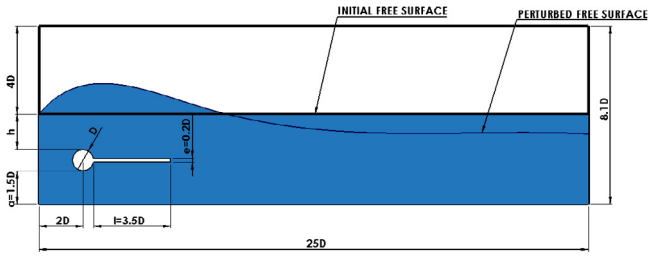

Fig. 1. Problem set up and main parameters.

This work combines on one hand the complexity of a viscous flow around a bluff body that contains a deformable structure on the wake, and on the other hand the complexity introduced by the presence of free surface. The combination of FSI phenomena and free surface deformation makes this problem very attractive from a computational point of view. Consequently, this work evaluates the influence of the sea surface on a typical fluid–structure interaction device such as that investigated by Turek et al. (2010). The present numerical study also shows an extensive investigation of effects of the dominant non dimensional numbers on the drag and lift of a cylinder and deformation of the plate. In the present computational methodology, both the structural dynamics and the fluid solver are based on finite volume discretizations. The computational methodology is verified and validated in one benchmark case: flow over a circular cylinder with a splitter plate such as in the case studied by Turek et al. (2010), and a second case where free surface is added to the problem, and consequently new non-dimensional numbers appear.

This paper is distributed as follows: the computational methodology is described in Section 2, while the flow configuration, main parameters and mesh description are introduced in Section 3. In Section 5, first, the methodology is verified and validated through the simulation of a benchmark problem, and second, the effects of the free surface on the splitter plate vibration, the drag and lift forces are discussed. Finally, concluding remarks are presented in Section 6.

2. Methodology

The two-way interaction between an elastic structure and an incompressible flow is studied in this work. A schematic representation of the problem appears in Fig. 1. The problem is considered to be two dimensional, therefore no deformations or displacements are allowed in the Z direction. The flow comes from the left part of the rigid cylinder. The structure is deformed by the pressure and the shear forces created around the splitter plate due to the vortex shedding produced by the cylinder. In those cases where two immiscible Newtonian fluids are involved in the problem, gravity force and free surface are added to the problem. In that situation, the structure formed by a cylinder with diameter D and a cantilever splitter plate of length l and width e, is submerged a distance h below the free surface that separates two immiscible fluids. Similarly to Reichl et al. (2005), the depth h is measured from the free surface to the top of the cylinder. Since free surface is present, gravity g is applied over the domain. An extended branch of the open source code OpenFOAM (2018), called OpenFOAM - extend 3.2, was used to solve this FSI problem. This code contains a fluid solver, an elastic solid solver and the possibility of coupling both parts. Both the fluid and the structural parts are discretized following the Finite Volume Method (FVM).

2.1. Fluid dynamics solver

The equations to be solved for the fluid part are the incompressible Navier–Stokes equations. As the Reynolds numbers investigated are moderate, we will consider laminar regime, and consequently no turbulence models have been included.

$$\nabla \cdot \mathbf{u}_f = 0 \tag{1}$$

$$\frac{\partial(\rho_f \mathbf{u}_f)}{\partial t} + \nabla(\rho_f \mathbf{u}_f \otimes \mathbf{u}_f) = \rho_f \mathbf{g} - \nabla p + \mu_f \nabla^2 \mathbf{u}_f \tag{2}$$

where $\mathbf{u}_f$ is the fluid velocity vector, p is the pressure field, ρ_f the fluid density and μ_f the fluid viscosity. Because two different immiscible fluids are considered, the density and viscosity change locally. The boundary conditions for the fluid part are: prescribed velocity profile for the inflow and no slip boundary conditions for the cylinder, the plate and the top and bottom walls. A zero-velocity gradient and zero-pressure condition was used for the outlet. A transient PISO algorithm (Pressure Implicit Splitting of Operators) implemented in OpenFOAM (2018) was used to solve the unsteady Navier–Stokes equations. This algorithm, which is an improved version of the SIMPLE algorithm, contains an additional corrector step with one predictive step and two correction steps, see Versteeg and Malalasekera (2007) and Oro (2012). For the time discretization, both a Euler and backward temporal second order discretization scheme were used, and very little differences were found. The convection term has been discretized using a second order upwind scheme.

The Volume of Fluid (VOF) method is based on the idea of a scalar fraction function α defined locally on each cell of the mesh whose value depends on the fraction of volume occupied by each fluid. As the two fluids A and B are separated by the free surface, the value of α is zero when a cell is filled with fluid A; $\alpha = 1$ when the cell is full of fluid B; and $0 < \alpha < 1$ when a cell is shared between both fluids and the interface divides the cell. The equation to model the volume fraction of one phase α, without mass sources or mass transfers between phases, is the following:

$$\frac{\partial \alpha}{\partial t} + \mathbf{v} \cdot \nabla \alpha = 0 \tag{3}$$

Once the fraction function α is known, the local values of the density and viscosity ρ_f and μ_f are computed accordingly for each finite volume.

2.2. Solid mechanics solver

For an arbitrary elastic body of volume Ω, bounded by surface Γ with unit normal $\mathbf{n}$, the conservation of linear momentum in integral form is given by

$$\underbrace{\frac{D}{Dt}\int_{\Omega} \rho_s \, \mathbf{u}_s \, d\Omega}_{\text{Acceleration}} = \underbrace{\oint_{\Gamma} \mathbf{n} \, \boldsymbol{\sigma} \, d\Gamma}_{\text{Surface Forces}} + \underbrace{\int_{\Omega} \rho_s \, \mathbf{b} \, d\Omega}_{\text{Body Forces}} \tag{4}$$

where $\mathbf{u}_s$ is the solid velocity, $\boldsymbol{\sigma}$ is the stress tensor, ρ_s is the solid density, and $\mathbf{b}$ is the body force per unit mass. A constitutive relation of a solid material essentially relates the material stresses to the material strains. In the current study, the body is assumed to be elastically isothermal, therefore thermal and plastic effects are neglected. An elastic solid undergoing large strains and large rotations is governed by the St. Venant-Kirchhoff hyperelastic constitutive relation (5). These equations are solved using the finite volume method.

$$S = 2\mu \mathbf{E} + \lambda(\mathbf{E})\mathbf{I} \tag{5}$$

where $\mathbf{E}$ is the Lagrangian tensor and $\mathbf{S}$ is the second Piola–Kirchhoff stress tensor.

$$\mathbf{E} = \frac{1}{2}(\nabla u + \nabla u^T + \nabla u \nabla u^T) \tag{6}$$

The Lame coefficients are μ and λ are related with the Young's modulus E and the Poisson ν. They are defined as:

$$\mu = \frac{E}{2(1+\nu)} \tag{7}$$

$$\lambda = \frac{\nu E}{(1+\nu)(1-2\nu)} \tag{8}$$

2.3. Coupling and interface considerations

The coupling algorithm that has been used to simulate the solid and fluid interaction is the Aitken algorithm. Based on our experience, this algorithm offers robustness and good convergence. Others algorithms such as IQN-ILS Degroote et al. (2009) could be used, but they are less robust.

The contact interface between the solid and the fluid must satisfy two basic conditions. The kinematic condition imposes the contact points between the fluid and the solid to have the same velocity. The second condition is the dynamic condition, which states the stress equilibrium between the fluid and the solid at the contact surfaces. These are:

$$\mathbf{u}_f = \mathbf{u}_s \tag{9}$$

$$\sigma^f \mathbf{n} = \sigma^s \mathbf{n} \tag{10}$$

where σ^f and σ^s are the stress tensors associated to the fluid and solid respectively. The constant z planes are considered to be symmetry planes, and the splitter plate in displacements and velocities interacts with the fluid mesh points. The left part of the structure is considered to be cantilevered and no deformations or displacements are allowed in the Z direction.

2.4. Dimensionless parameters

We consider the general case where two different fluid phases are present and an averaged upstream velocity $\overline{U}$ interacts with the structure. In our case, the solid is submerged in the bottom phase with density ρ_f^b and viscosity μ_f^b. The top phase has density $\rho_f^t < \rho_f^b$ and viscosity μ_f^t. The material considered for the flexible structure, is a combination of two rubber-like materials such as polybutadiene and polypropylene with global density ρ_s, Young's modulus E and Poisson coefficient ν^s. Due to the very low stiffness of the materials used here, large deformations of the structure are possible.

Table 1
Number of cells of each subdomain, fluid and structural and cell size close to the beam (A_h/D^2). The total number of cells (structure+fluid) in Turek and Hron (2007) mesh is also included for reference.

Mesh	Cells structure domain	Cells fluid domain	A_h/D^2
1	1000	11 554	6.09e−3
2	1250	17 924	3.06e−3
3	1500	21 774	2.03e−3
Turek and Hron (2007)	19 488		

Assuming that the geometry and fluid property ratios are fixed, the non dimensional parameters e/D, l/D, $\rho_f^b/\rho_f^t = 1000$ and $\mu_f^b/\mu_f^t = 67.57$ will not be changed throughout this work. According to the dimensional analysis theorems, the problem can be studied in terms of the following non dimensional numbers: the Reynolds number (Re), the Froude number (Fr), the Cauchy number (Cy), the mass ratio (M) and the geometrical parameter h/D that controls the free surface influence.

$$Re = \frac{\rho_f^b \overline{U} D}{\mu_f^b} \qquad C_y = \frac{\rho_f^b \overline{U}^2}{E} \qquad Fr = \frac{\overline{U}}{\sqrt{gD}} \qquad M = \frac{\rho_f^b}{\rho_s} \tag{11}$$

Other authors such as Shukla et al. (2013) use the non-dimensional bending stiffness parameter $k_B = 2EI/\rho_f^b U^2 l^3$ instead of the Cauchy number, where EI is the flexural rigidity of the plate. The relation between both parameters in 2D problems is $k_B = \frac{1}{6C_y}(\frac{e}{l})^3$.

3. Problem description

In this work two cases have been studied and compared. In the first case, the geometry and the parameters proposed by Turek et al. (2010), were studied. The cases pose two typical two-way FSI problem where an elastic rectangular structure is deformed by the pressure and shear forces created in the surroundings of the splitter plate due to the effect of the flow separated around the cylinder. The geometry used in the first case has similar dimensions to the one presented in previous literature, where the rectangular domain has $4.1D$ and $25D$ with the thickness $0.5D$, with the cylinder diameter being $D = 0.1$ m. The circular cylinder has its centre placed at point $(x_c, y_c) = (0.2, 0.2)$ m. The dimensions of the flexible structure are $3.5D$ by $0.2D$. A test point named A is defined at the position $x = 6D, y = 2D$, and will be considered as the reference point for measuring the displacement of the splitter plate. Once the comparison against Turek et al. (2010) has been completed, the following step will be the study of the same problem, but adding free surface and varying the dimensionless numbers. As shown in Fig. 1, an additional rectangular domain $25D$ long, $4D$ wide and filled with air has been added on the top of the previous geometry proposed by Turek et al. (2010).

The depth of the structure is changed by varying the distance h from the free surface to the top of the cylinder, see Fig. 1. In order to study the case $h/D = 2.1$, avoiding domain influences on the structure, the geometry was increased from the bottom part $2D$ as the proposed by Zhang and Shi (2016).

In the validation case, the benchmark from Turek and Hron (2007) or Turek et al. (2010), has an inlet velocity with a parabolic profile and a mean velocity $\overline{U} = 2$ m/s, defined as

$$U = \frac{3}{2}\overline{U}\frac{y(H-y)}{(\frac{H}{2})^2}, \tag{12}$$

where $H = a + h + D$. For the second multiphase case, where the cylinder and the elastic plate are both submerged under the denser fluid in the presence of a gravity field and the free surface, the parabolic profile will be changed for a mean velocity $\overline{U} = 2$ m/s.

3.1. Mesh description

Different meshes have been studied in order to accurately measure the forces acting on the structure, and that has required a high number of cells in the mesh. In order to capture the tension and compression zones, it is absolutely necessary to use more than 4 cell in the transverse section of the splitter plate even having a very small thickness, see Fig. 2 where the solid computational domain is presented. Three different structured meshes were used for the purpose, see Fig. 3 as an example. In order to validate mesh convergence, the number of cells on the cylinder and on the splitter plate have been varied. As shown in Fig. 4, the number of cells in the x and y boundaries of the geometry needs to perfectly match the number of cells in the splitter plate and cylinder. The same happens in the cases in which the air domain is added to the top. The number of cells for the solid and fluid parts of the three different meshes are listed in Table 1. The horizontal displacement of point A, initially at $(6D, 2D)$ referred to as X, is an order of magnitude smaller than the vertical displacement Y. A mesh convergence process based on the non dimensional tip displacement is presented in Table 2.

Table 2
Comparison between different meshes and different time steps with the benchmark case.

Mesh	$\frac{\Delta t\overline{U}}{D}$	X/D	Y/D	$\frac{f_x D}{\overline{U}}$	$\frac{f_y D}{\overline{U}}$	% relative error in Y/D
Turek and Hron (2007)	1e−2	0.0285	0.3563	0.5375	0.2686	–
1	1e−2	0.02495	0.3607	0.5375	0.2686	1.01
2	1e−2	0.02684	0.3662	0.5375	0.2686	1.02
3	1e−2	0.02853	0.3676	0.5375	0.2686	1.03
3	2e−2	0.02765	0.3682	0.5375	0.2686	1.03

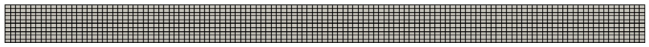

Fig. 2. Schematic of the solid computational domain.

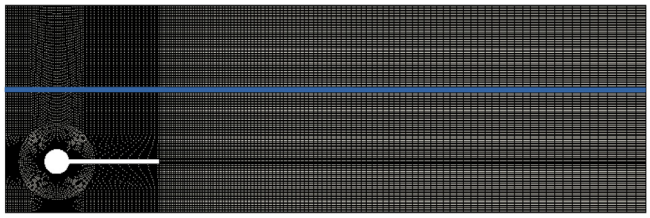

Fig. 3. Structure and general view of the mesh 2 for the free surface case. The blue line indicates the initial free surface when two fluids are simulated.

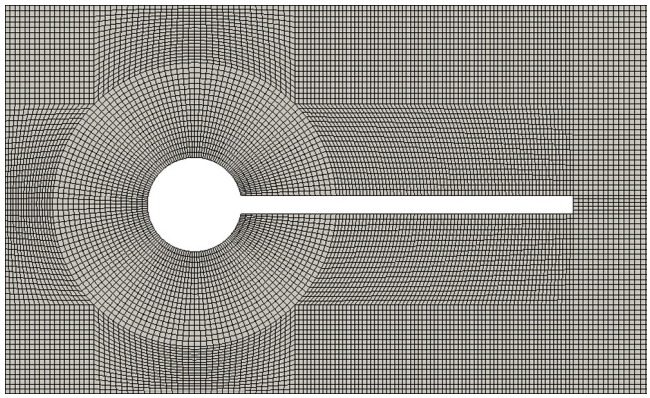

Fig. 4. Zoom of the mesh 2 over the cylinder and splitter plate.

A time step convergence process has been carried out using different time steps. Time steps $\frac{\Delta t\overline{U}}{D} = 2e{-}2$ and $\frac{\Delta t\overline{U}}{D} = 1e{-}2$ have been considered for both the structure and fluid parts, showing differences under 1%, see Table 2. It is worth stressing that the same time step has been used for both the structure and fluid parts.

4. Validation

Before studying the influence of the free surface on the case described in Section 3, some previous tests have been performed to assess the validity of the numerical procedures. The validation cases are the ones proposed by Turek et al. (2010), which in fact, have been studied by other authors such as Gallegos and Sharma (2016) and Bhardwaj and Mittal (2012). Two different cases, FSI 2 and FSI 3 from now on, have been run. The main results monitored are the displacements of the tip of the splitter plate (point A), the total drag and lift forces acting on the structure (formed by both the cylinder and the splitter plate) and the dominant frequency of the splitter plate oscillations.

4.1. Main validation cases (FSI2 and FSI3)

The two different sets of parameters for cases FSI2 and FSI3, used for the validation exercise as in Turek et al. (2010) appear detailed in Table 3. The case presented in Turek et al. (2010) is based on a single fluid arrangement. The differences

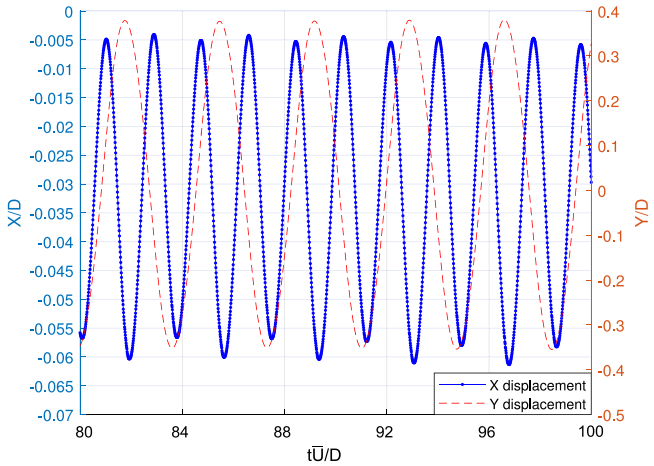

Fig. 5. Horizontal and vertical time-varying displacements of point *A*.

Table 3
Parameters used in the FSI2 and FSI3 validation cases.

Parameter	FSI 2	FSI 3
ρ^s $[\frac{kg}{m^3}]$	10^4	10^3
ν^s	0.4	0.4
ρ^f $[\frac{kg}{m^3}]$	10^3	10^3
ν^f $[\frac{m^2}{s}]$	10^{-3}	10^{-3}
$\overline{U}$ $[\frac{m}{s}]$	1	2
E [Pa]	$1.4 \cdot 10^6$	$5.6 \cdot 10^6$
Re	100	200
Cy	$7.14 \cdot 10^{-4}$	$7.14 \cdot 10^{-4}$
M	0.1	1

Table 4
Comparison between the amplitudes and frequencies of the horizontal and vertical displacements of point *A* (splitter plate tip), obtained by Turek et al. (2010) and Pisacreta (2017), for case FSI3.

Benchmark case **FSI3**	X/D	Y/D	$\frac{f_x D}{\overline{U}}$	$\frac{f_y D}{\overline{U}}$
Turek et al. (2010)	0.0285	0.3563	0.5375	0.2686
Pisacreta (2017)	0.0252	0.3516	0.5495	0.2705
Present work	0.0268	0.3662	0.5375	0.2686

between cases FSI2 and FSI3 are therefore, the elastic properties of the solid, the average inflow velocity and the density of the elastic part, which clearly affects the inertial forces acting on the moving plate, this last property being the most significant difference between both test cases. The time-varying displacement of tip of the plate follows a sinusoidal pattern. Although the vertical displacement is dominant (see Fig. 5), the horizontal displacement of the tip has been also compared to the results available in the literature.

The amplitudes and frequencies of the horizontal and vertical displacement of point *A* in case FSI3, appear in Table 4 for comparison with the results obtained by Turek et al. (2010). In all the results presented in this work, the peak amplitude of the vertical displacement *Y* has been used and compared to the value obtained using $\sqrt{2}$ of the root mean square (RMS) of the signal, showing practically no difference. The results presented by Turek et al. (2010) derive from a convergence test based on the number of cells in the mesh and the time step used for the computations. In the work presented here, for comparison purposes, results derive from a mesh with a similar number of cells and time step. These are also similar to those used by Pisacreta (2017). Table 4 shows that no significant differences have been found. In the second validation case FSI2, results are compared to the work by Turek and Hron (2007), and additionally to the results found in Gallegos and Sharma (2016), obtained using the commercial software ANSYS.

Fig. 6 shows the instantaneous vorticity fields around the cylinder and how the vortex shedding induces the periodic vibration of the splitter plate. The vorticity field is shown in dimensionless form, defined as $\omega_z^* = \frac{\omega_z D}{U_\infty}$, where ω_z is the out of plane vorticity. The diameter of the cylinder determines the size of the wake structures generated, and consequently it influences the vertical amplitude of the plate. The shear layers appear elongated and after separating from the cylinder

Table 5
Comparison between of the amplitudes and frequencies of the horizontal and vertical displacements of extreme plate point A and the Hron–Turek results (Turek et al., 2010) for case FSI2.

Benchmark **FSI2**	X/D	Y/D	$\frac{f_x D}{\overline{U}}$	$\frac{f_y D}{\overline{U}}$
Turek and Hron (2007)	0.1203	0.787	0.38	0.20
Gallegos and Sharma (2016)	0.1192	0.790	0.382	0.196
Present work	0.1057	0.778	0.39	0.1953

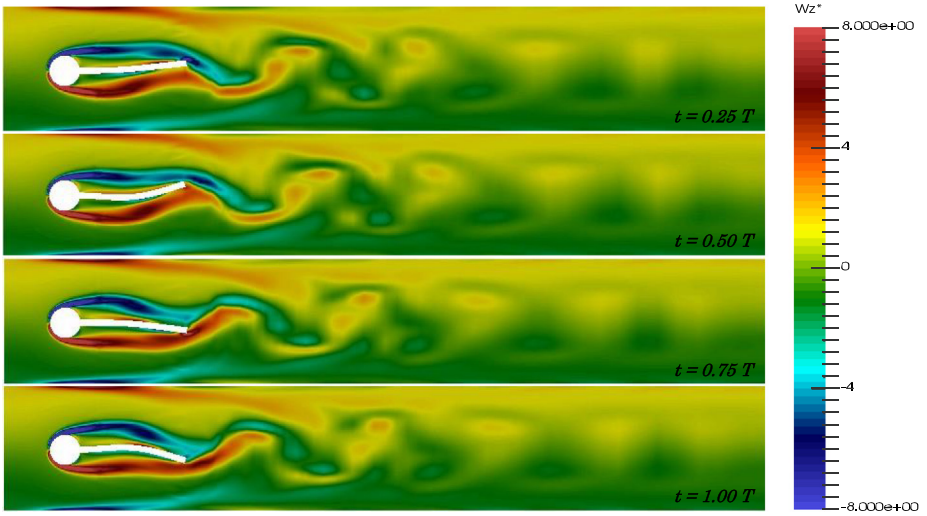

Fig. 6. Instantaneous vorticity snapshots during a complete vortex shedding cycle of period T. Clockwise vorticity appears in blue (down to $\omega^*_{z_{min}} = -8$) and counter-clockwise in red (up to $\omega^*_{z_{max}} = 8$). Vorticity is presented in dimensionless form, defined as $\omega^*_z = \frac{\omega_z D}{U_\infty}$. (For interpretation of the references to colour in this figure legend, the reader is referred to the web version of this article.)

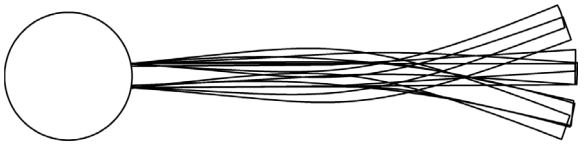

Fig. 7. Superimposed view of the deflections of the splitter plate.

surface, they reattach at the surface of the splitter plate, which avoids their interaction as in the classical vortex street formation. After a transient flow determined by the initial conditions where the plate exhibits little deformation, the motion of the plate reaches a periodic self-sustained oscillation with practically constant amplitude. The deformation of the plate can be seen in Fig. 7, where eight different deflected shapes taking place during a full oscillation cycle appear superimposed. The deformations resemble those similar to the second mode of vibration of a cantilevered beam. The results in Tables 4 and 5, show how there is an accordance between the computations presented here and the results by Turek et al. (2010) and Pisacreta (2017).

Notwithstanding, the FSI3 benchmark case is highly sensitive due to the great difficulties in obtaining a numerically stable solution. Phenomena such as inertial effects and mesh distortion must be avoided during the fluid and the structural coupling, especially during the transient part of the simulation. The integration of the different schemes must be performed in such a way that both solvers accept the solution provided by the other, and generate a coherent solution. The number of coupling iterations required to obtain convergence between both codes depend basically on how much the beam deforms. Excessive time steps imply large deformations and distortions in the mesh structure that yield errors during the calculation. During the transient part, where unexpected inertial effects might appear, the use of a very large number of internal iterations for fluid-structural coupling could be inefficient and divergent. Regarding the mesh distortion problems that might appear when parts of the structure suffer large accelerations, we must clarify that OpenFOAM-extend does not implement any re-meshing algorithm. The only possibility when the deformation of the mesh is excessive is the implementation of a quadratic or linear Laplace solver that smooths the node positions and prevents inconsistent cells.

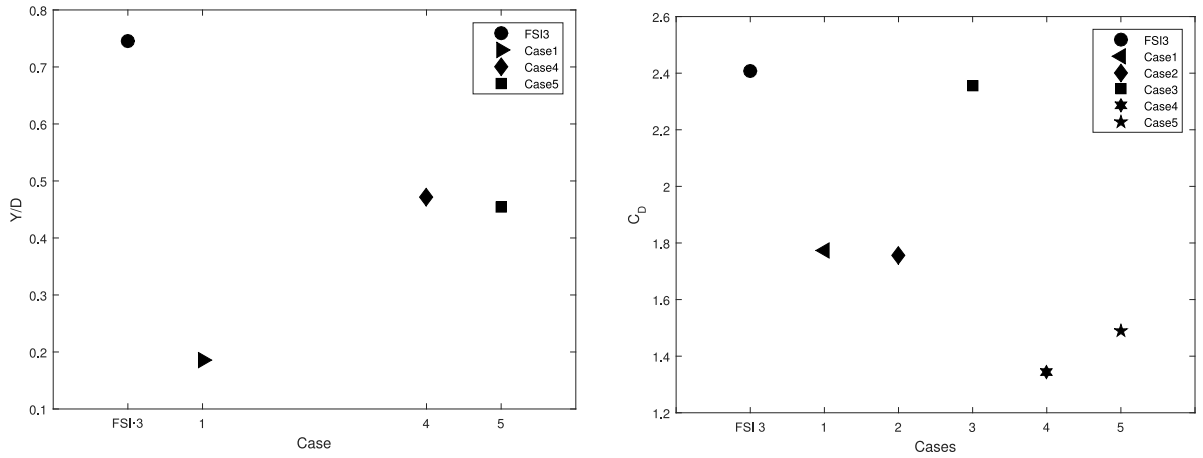

Fig. 8. Comparison of the amplitude displacement (left) and drag force coefficient (right) for some the additional cases. Case 0: Turek case FSI 3. Case 1: Turek case FSI 3, but using uniform inflow profile $U = 2$. Case 2: Case 1 with a rigid splitter plate. Case 3: Turek case FSI 3, but using a rigid splitter plate. Case 4: The top wall is set at $10.1D$ from the cylinder centre, and the bottom wall is set at $6D$ from the cylinder centre. Uniform inflow profile $U = 2$. Case 5: The top wall is set at $10.1D$ from the cylinder centre, and the bottom wall is set at $2D$ from the cylinder centre. Uniform inflow profile $U/\overline{U} = 1$.

4.2. Sensitivity analysis of the validation cases FSI2 and FSI3

In order to test the sensitivity of these results to the particular parameters and boundary conditions selected for cases FSI2 and FSI3, five additional cases were also studied. All of them have the same fluid and solid properties as case FSI3. The additional cases are:

- Case 1. Corresponds to the FSI 3 (Turek et al., 2010), but using uniform inflow profile $U/\overline{U} = 1$.
- Case 2. Same as Case 1, but using a rigid splitter plate.
- Case 3. Similar to FSI3 (Turek et al., 2010), but using a rigid splitter plate.
- Case 4. The top wall is set at $10.1D$ from the cylinder centre, and the bottom wall is set at $6D$ from the cylinder centre. Uniform inflow profile $U/\overline{U} = 1$.
- Case 5. The top wall is set at $10.1D$ from the cylinder centre, and the bottom wall is set at $2D$ from the cylinder centre. Uniform inflow profile $U/\overline{U} = 1$.

In case 1, the parabolic inflow is substituted by a uniform flow equal to the average value of the parabolic case. In the second and third cases, the elastic plate is replaced by a rigid one to measure the variation of the forces on the structure. Finally, in the last two cases the geometry is modified in order to evaluate the influence of blockage. In case 4 both walls are separated from the structure, and in case 5 only the bottom wall is separated while the other remains at the same position as in FSI3.

The amplitude of the vertical displacement of the tip in cases 1, 4 and 5 appears in Fig. 8. As expected, using a uniform profile instead of the parabolic one used in FSI3 creates less deformation on the plate. When comparing case 1 with cases 4 and 5, where the width of the channel is enlarged, we observe that the blockage effect of the top and bottom walls reduces the plate motion. This effect is inferred from the results presented in Zhang and Shi (2016), where the blockage effect was studied in a rigid version of the structure presented here. They showed that blockage clearly affects the frequency of the vortex shedding behind the structure, as well as the amplitude oscillation of the lift coefficient. Drag forces appear in Fig. 8 for all cases studied. According to the values obtained, there is not an important drag difference between the elastic and the rigid plate versions, with the FSI3 and case 3 having similar values when the inflow is parabolic, or cases 1 and 2 for a uniform inflow. When the distance between the horizontal walls and the structure is enlarged, and consequently the blockage effect is reduced, the drag is also reduced with respect to the other cases. The dependence of the drag coefficient on the blockage effect was also studied by Zhang and Shi (2016). Some of the results obtained in this validation exercise, will be used as reference values in Section 5, where the free surface is added to the problem.

5. Results

With the numerical procedures fully validated, in this section the free surface and the gravity field are added to the problem. The goal is to investigate the effect of this discontinuity on the splitter plate dynamics and its excitation. In order to have a reference framework, the structure is analysed using fluids with the same characteristics as those used for the benchmark cases, namely glycerine and air at the upper part of the domain, see properties in the FSI3 case Table 3

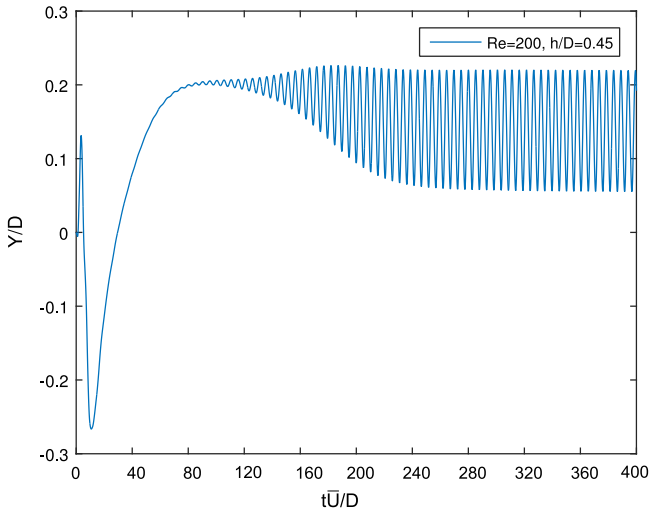

Fig. 9. Evolution of vertical displacement of the tip of the plate corresponding with Reynolds number $Re = 200$, Froude number $Fr = 2$, Cauchy number $Cy = 7.14e{-}4$ and $h/D = 0.45$.

and density and viscosity ratios in Section 2.4. The non-dimensional parameter h/D will be increased from 0.3 up to 1.6, where the distance between the upper part of the cylinder and free surface (at rest), is equal to the distance to the top wall in the benchmark cases.

The effects of fluid viscosity (Reynolds number), splitter plate stiffness (Cauchy number) and the gravity field (Froude number) on the dynamics and the excitation are studied in detail in order to provide a complete perspective of the problem. The mass ratio M (structural mass upon displaced fluid mass) will be kept constant and equal to 1, for all cases so the influence of buoyancy is kept away from the problem.

5.1. Splitter plate deformation in the presence of free surface

Initially the study is focused on the study of the effect of the distance to the free surface on the deformations of the splitter plate. Variations in the Reynolds number (fluid viscosity), Cauchy number (splitter plate flexural stiffness) and Froude number (gravity field) are introduced at the same time as varying h/D. Fig. 9 shows the typical time series of the displacement of the tip of the splitter plate in one of the numerical experiments, run with $Re = 200$, $Fr = 2$, $Cy = 7.14 \cdot 10^{-4}$ and $h/D = 0.45$. Three time windows can easily be identified in the figure. First, the splitter plate deforms until it reaches its equilibrium position, in this case at a $t \sim 4$ s, due to the presence of the free surface which implies absence of symmetry in the vertical direction. Afterwards, the vortex shedding starts to change the pressure field leading to very small oscillations ($4 \text{ s} < t < 12$ s) until it reaches a self-sustained oscillation with constant amplitude for $t > 12$ s.

Another important aspect is the influence of the proximity to the wall (a/D). The tip amplitudes for a run with parameters $h/D = 1.6$, $Re = 200$ and $Cy = 7.14 \cdot 10^{-4}$ appear in Fig. 10. The figure allows to conclude that the tip amplitude barely changes if a/D is over a certain value.

5.1.1. Effect of Reynolds number

A series of simulations were carried out changing the Reynolds number in order to understand the influence of this parameter on the plate dynamics. The physical magnitude that was used to change the Reynolds number is the kinematic viscosity. Here, the rest of dimensionless numbers in the problem, such as the Cauchy and the Froude number, will be kept constant with the values: $Cy = 7.14 \cdot 10^{-4}$ and $Fr = 2$. The Re is varied from a value of 100, with no tip displacements observed, to a value of 1000. Note that with a $Re = 1000$, if a fine mesh is used, turbulence modelling can be avoided. In Fig. 11, the vertical displacement of the tip of the splitter plate (point A) is represented against depth, for the different Reynolds numbers investigated. One of the reference cases from Section 4.2, Case 4 with uniform inflow velocity $U/\overline{U} = 1$ and $Re = 200$ but with structure immersed in a single fluid (properties defined in the case FSI3 Table 3), has been included for comparison. This reference case is indicated in the figure using a horizontal dashed line. Re appear indicated using symbols.

The plot shows how there is a critical Reynolds number within the interval $Re = [100, 150]$, at which the tip motion starts. In all cases, increases in Reynolds number result in increases of the splitter plate oscillations. This trend was also observed in the validation case FSI3 Pisacreta (2017). In fact the plot shows how amplitude in all curves increase monotonically with depth until a point at which it saturates, and depth starts to have small influence on it. For example,

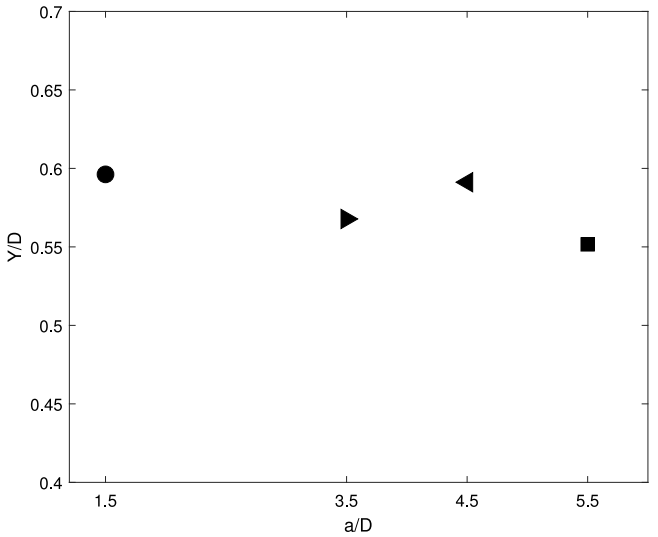

Fig. 10. Vertical amplitudes of the plate tip versus distance to the bottom wall a/D. The Froude $Fr = 2$ and the Cauchy numbers $Cy = 7.14 \cdot 10^{-4}$ are kept fixed.

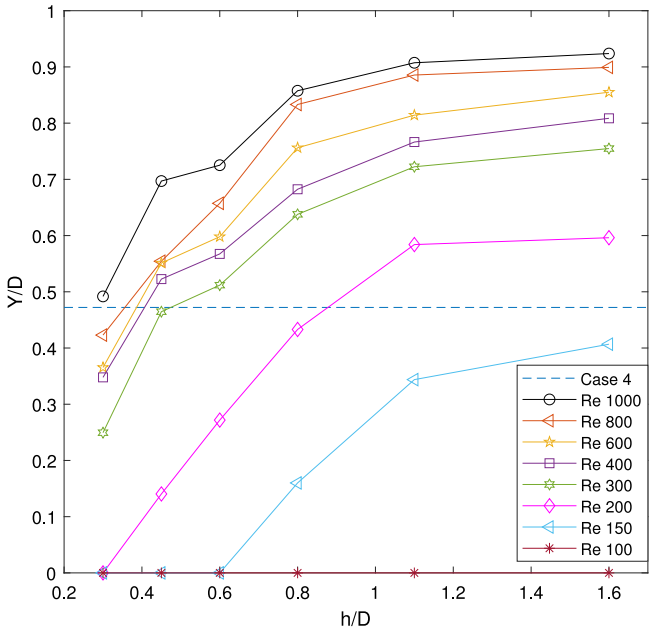

Fig. 11. Vertical amplitudes of the plate tip versus depth for different Reynolds number values. The Froude $Fr = 2$ and the Cauchy numbers $Cy = 7.14 \cdot 10^{-4}$ are kept fixed. Case 4, with uniform inflow velocity $U/\overline{U} = 1$ and FSI3 properties (Table 3), has been included for comparison in a dashed blue line.

in the case of a $Re = 200$, it is around an h/D of 1.1. The growth of the amplitude with h/D is a consequence of the asymmetry created by the gap flow between the free surface and the structure, that ultimately modifies the vorticity and pressure distributions in the wake of the system. Analogously to the rigid plate case (Zhang and Shi, 2016), the free surface acts as a deformable wall able to alter the vortex generation in the gap region. In Figs. 12 and 13, two dynamic pressure contour maps are shown for depths $h/D = 0.8$ and $h/D = 1.6$. In the plots, the pressure of the upper fluid is not coloured for an easier identification of the free surface. The pressure is presented in dimensionless form, with $p^* = \frac{p}{\rho \overline{U}^2}$.

The proximity of the free surface modifies the pressure field around the structure and consequently affects the dynamic pressure acting on the plate. To have a clearer image of the dynamic pressure role on the plate deformation, the differences in dynamic pressure between both sides of the plate has been plotted for three different depths h/D of 0.45, 0.8 and 1.6, when the tip of the plate is at its highest and at its lowest position, see Fig. 14. The cases with the larger depth imply

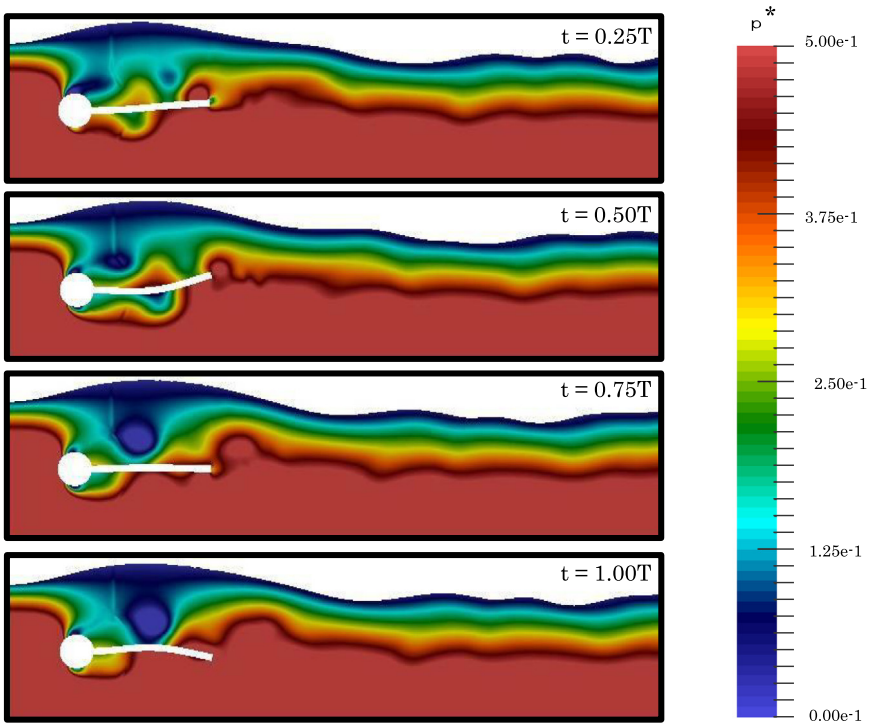

Fig. 12. Snapshot of the normalized pressure field contour plot at $h/D = 1.6$ during a complete shedding cycle of period T. The rest of parameters are: $Fr = 2$, $Cy = 7.14 \cdot 10^{-4}$ and $Re = 200$.

larger dynamic pressure differences over the splitter plate hence, larger deformations. The free surface acts as a damper that prevents large oscillation amplitudes on the plate, dissipating part of the energy in wave formation.

Regarding the vorticity field, two runs consisting of 4 snapshots from a full oscillation cycle, are presented for two cases with different h/D, in Figs. 15 and 16. The proximity of the free surface yields a reduction of the oscillatory character of the wake, and generates a flow deflection towards the opposite side of the free surface. When the structure is near the free surface, the lower shear layer seems not to reattach to the splitter plate. The wave generated on top of the structures, imposes a lower pressure region as seen in Figs. 12 and 13, that forces a modification of the separation point on the upper surface of the cylinder. Under this situation, the upper shear layer is heavily conditioned by the wave shape and detaches from the cylinder at a considerably larger angle if compared to that in the lower part.

In order to understand better the effect of depth on the plate dynamics, a numerical experiment falling in the part of Fig. 11 in which the tip amplitude grows monotonically ($h/D = 0.45$ and $Re = 200$), therefore showing a large effect of the free surface, is analysed here. Selected points for the analysis are presented in Fig. 17 on top of the time series of the displacement of this particular case. In order to confirm the periodicity of the dynamic pressure field, points such as P_1 and P_9 are selected in the same part of the curve, but in a different oscillation cycle. The dimensionless dynamic pressure field ($p* = \frac{p}{\rho \overline{U}^2}$) corresponding to each of the points described, appear in Fig. 18. The dynamic pressures at both sides of the splitter and the pressure difference are presented in Fig. 19.

The evolution of the dynamic pressure field represented in Fig. 18 shows that a low dynamic pressure region is formed at the top part of the structure. This low pressure region reminds a recirculation area that is consistently placed below the highest part of the quasi steady wave. The recirculation area changes its shape during the simulation, as can be seen in the first four snapshots of Fig. 18. Moreover, this is indicated by the fact that the dynamic pressure difference curves in Fig. 19, evolve as a wave travelling from left to right, and it is in snapshot P5 of Fig. 18, that a second pressure difference peak appears. The last is near the tip of the plate whilst the first is located at a position $x/D \approx 1$. In snapshots P5 to P8 of Fig. 18, these two pressure difference peaks move to the tip until one of them vanishes yielding a pressure different in snapshot P9, very similar to that in P1, with the cycle starting again.

5.1.2. Effect of Cauchy number

In this subsection the dependence of the splitter plate dynamics on the Cauchy number is studied, see Eq. (11). Variations of this non-dimensional number have been achieved by altering the Young's elastic modulus E of the splitter plate, while keeping the Reynolds and Froude numbers constant with values of 200 and 2, respectively. The range of Cauchy numbers tested goes from $5.6 \cdot 10^{-5}$ to $1.1 \cdot 10^{-3}$, including in this range the one used during the benchmark case

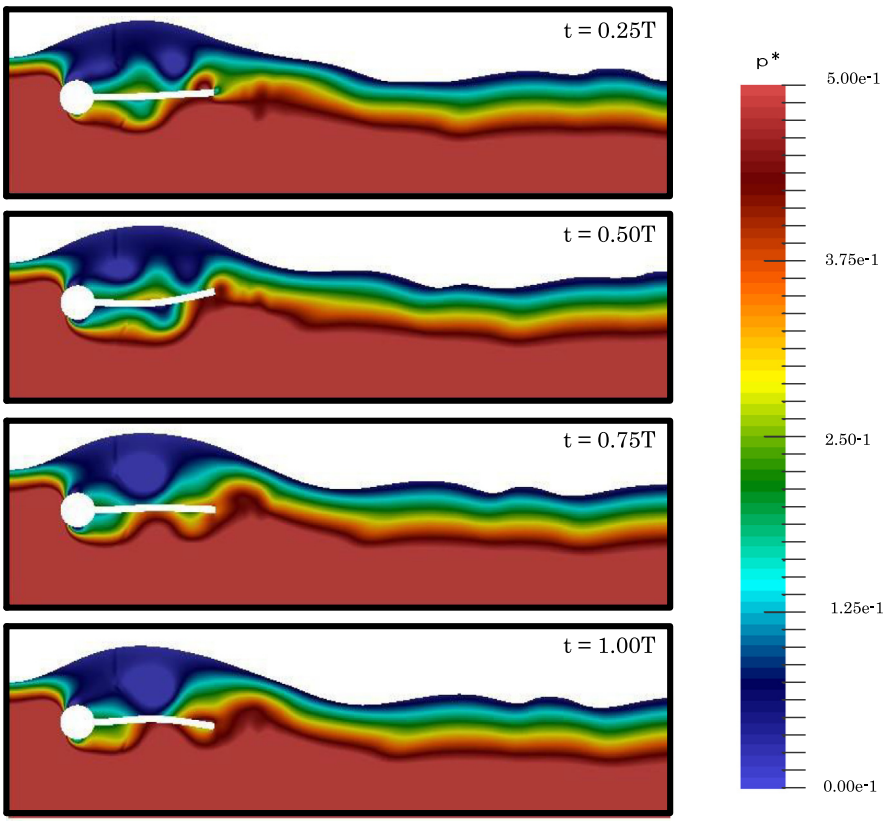

Fig. 13. Snapshot of the normalized pressure field contour plot at $h/D = 0.8$ during a complete shedding cycle of period T. The rest of parameters are: $Fr = 2$, $Cy = 7.14 \cdot 10^{-4}$ and $Re = 200$.

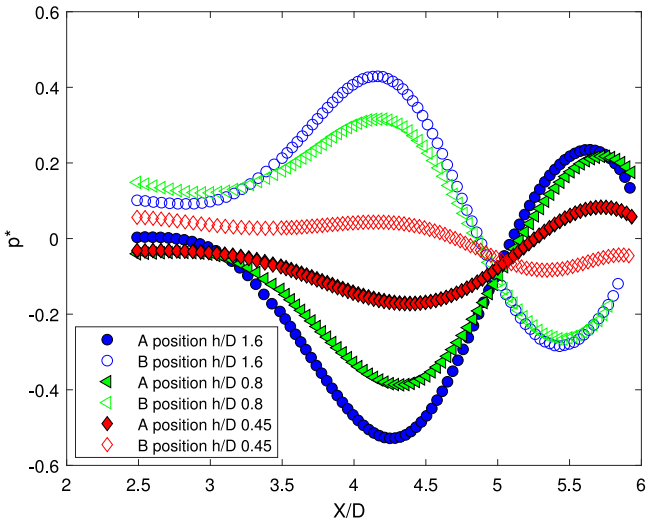

Fig. 14. Pressure field difference along the plate for three different depths, when the tip of the plate is at the highest (A) and lowest (B) positions. The Froude (**Fr** $=$ **2**) and the Cauchy numbers (**Cyz** $=$ **7.14e**$-$**4**) are kept fixed.

with $Cy = 7.14 \cdot 10^{-4}$. Lower Cauchy numbers imply very little deformations, and higher Cauchy numbers make stable computations very difficult because of large mesh distortions.

The results obtained show that for a fixed h/D, if the stiffness of the plate is increased (higher Young's modulus and lower Cauchy number), the amplitude of the tip decreases, see Fig. 20. The plot includes the reference case used in Fig. 11,

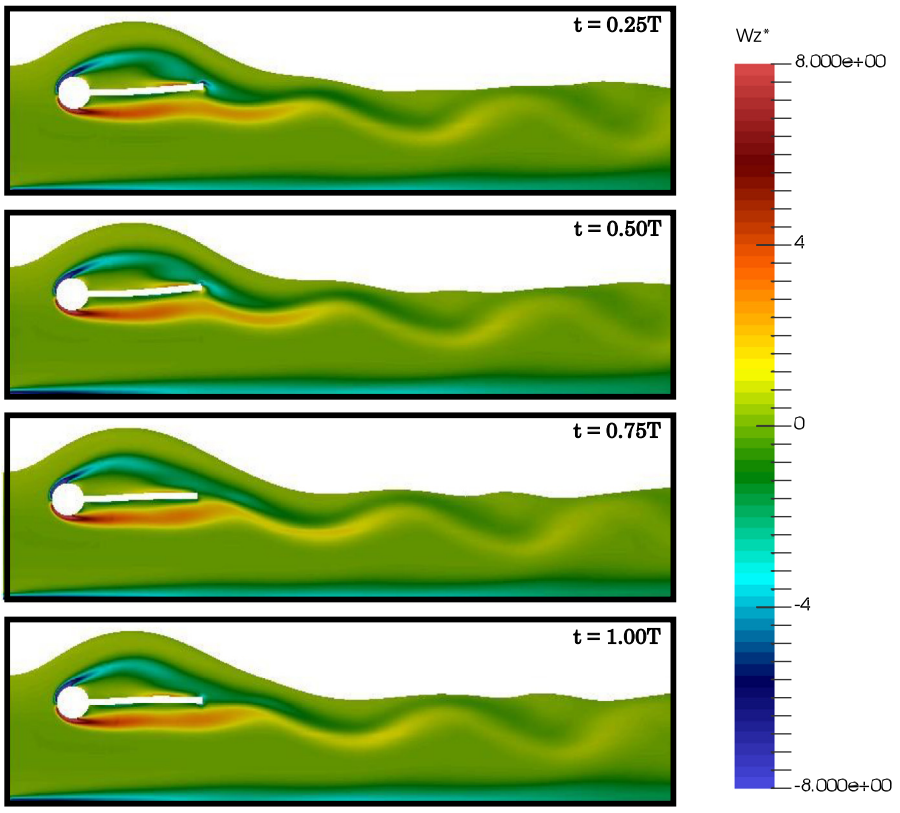

Fig. 15. Snapshot of the vorticity field contour plot at h/D = 0.45 during a complete shedding cycle of period T. Clockwise vorticity appears in blue (down to $\omega^*_{z_{min}} = -8$) and counter-clockwise in red (up to $\omega^*_{z_{max}} = 8$). The rest of parameters are: $Fr = 2$, $Cy = 7.14 \cdot 10^{-4}$ and $Re = 200$. (For interpretation of the references to colour in this figure legend, the reader is referred to the web version of this article.)

showing a single fluid computation (case 4) with $Cy = 7.14 \cdot 10^{-4}$, depicted with a dashed line. The same behaviour was also observed in the validation case FSI3 presented in Section 4.1 (Pisacreta, 2017), with the amplitude decreasing as the Young modulus was increased. When higher stiffness is imposed to the plate, $Cy \leq 5.26 \cdot 10^{-4}$, the system is unable to reach the amplitudes obtained without free surface for our range of depths. The oscillation amplitude of the point A increases with h/D, and the vertical amplitude tends to an asymptotic value when the structure is moved away far from the free surface influence. We can see here the same free surface damping. It is also worth noting that the plate remains stationary when depth is $h/D = 0.3$ for all the stiffness tested. This is interpreted as the existence of a critical depth where the pressure difference between both sides is unable to break the stability of the plate for the range of Cauchy numbers tested. A linear dependence of the amplitude of the splitter plate with Cauchy number for the different depths, appears in Fig. 21.

5.1.3. Effect of Froude number

In this case, the parameter varied in order to study the influence of the Froude number on the splitter plate dynamics, see Eq. (11), is the gravity acceleration. The rest of the non-dimensional numbers, such as Reynolds, mass and Cauchy numbers will be kept constant with values: $Re = 200$, $Cy = 7.14 \cdot 10^{-4}$ and $M = 1$. The range of Froude numbers studied goes from 2 to 3.5. The lower limit $Fr = 2$, corresponds to the realistic case where $g = 9.8$ m/s^2. Froude number higher than 3.5 were not examined due to the clear asymptotic behaviour of the plate oscillations found, see Fig. 22. Again reference case 4, with uniform inflow velocity $U/\overline{U} = 1$ and FSI3 properties (Table 3), has been included using a dashed line, for comparison. From Fig. 22, it is clear how Froude number amplifies the splitter plate oscillations. For $Fr \geq 2.5$, all the iso-Froude curves tend to converge to the same amplitude level, meaning that at this stage, there is very little influence of the Froude number on the plate dynamics, therefore inertial terms are more important than gravitational ones. For the smallest depth tested, $h/D = 0.3$, the data suggests that there is a critical Froude number in the interval $[2, 2.5]$ if any plates motions are to be observed. The absence of free surface decreases the vertical oscillation amplitude when compared to the gravitational cases for $Fr \geq 2.5$.

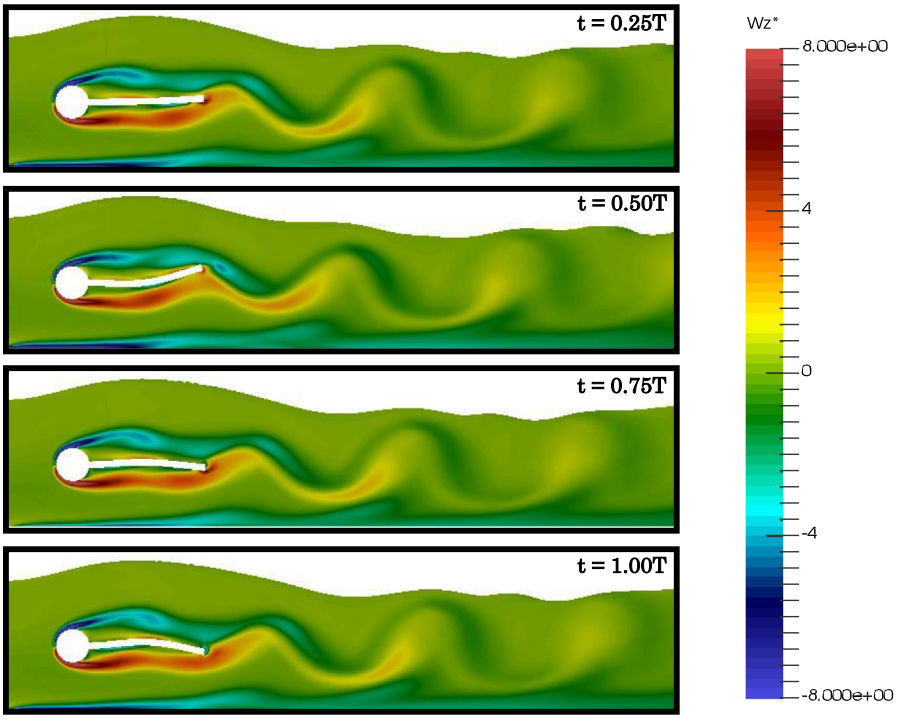

Fig. 16. Snapshot of the vorticity field contour plot at h/D = 1.60 during a complete shedding cycle of period T. Clockwise vorticity appears in blue (down to $\omega^*_{z_{min}} = -8$) and counter-clockwise in red (up to $\omega^*_{z_{max}} = 8$). The rest of parameters are: $Fr = 2$, $Cy = 7.14 \cdot 10^{-4}$ and $Re = 200$. (For interpretation of the references to colour in this figure legend, the reader is referred to the web version of this article.)

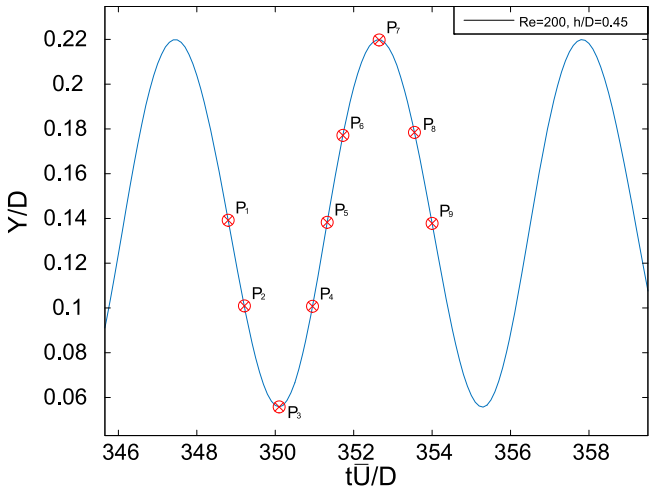

Fig. 17. Vertical periodic displacement signal of point A for $Re = 200$ and $h/D = 0.45$. Different positions $P_i \quad i = 1, \ldots, 9$ at different instants during one period have been selected for analysis.

5.2. Drag forces on the submerged structure in the presence of free surface

In this section, the fluid forces acting on the whole structure, including the cylinder and the splitter plate, are studied by varying the dimensionless numbers in the same way as in the previous section. Both, pressure and viscous forces will be integrated over the structure surface, and projected on the horizontal axis to obtain the drag force F_x. In order to compare different cases, and taking into account the oscillatory nature of these forces, a time average of the force components is

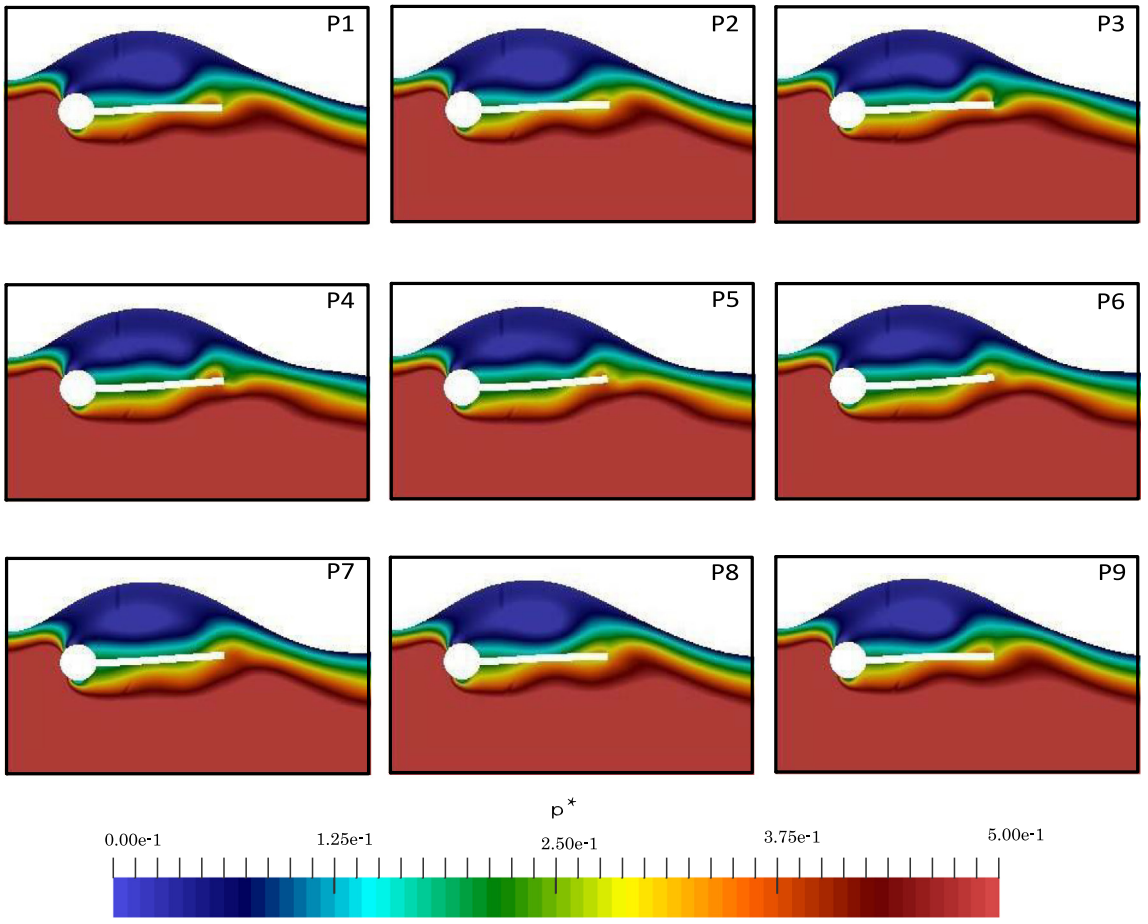

Fig. 18. Contour normalized pressure field snapshots.

calculated once a quasi periodic oscillation regime is obtained. These forces will be non-dimensionalized using Eq. (13).

$$C_D = \frac{F_x}{\frac{1}{2}\rho_f \overline{U}^2 cD} \tag{13}$$

5.2.1. Effect of Reynolds number

Similarly to what was performed in Section 5.1, several simulations were carried out changing the Reynolds number value $Re \in [100, 1000]$ in order to understand the influence of this parameter on the plate forces. The other non dimensional numbers were kept constant as $Cy = 7.14 \cdot 10^{-4}$ and $Fr = 2$ during the simulations.

A dashed line is included in Fig. 23, reference case 4, with uniform inflow velocity $U/\overline{U} = 1$ and FSI3 properties (Table 3), to allow comparisons. A reduction of the horizontal force F_x takes place when the Reynolds number is increased in this laminar range as a consequence of a decrease of the viscous component of the force. This trend is similar to that of the drag coefficient of an isolated cylinder for Reynolds numbers increasing in the same range. In terms of depth, the drag value increases linearly for all Reynolds numbers. This was previously reported by Bouscasse et al. (2017), with a Froude number of 2, when the authors studied the case of an isolated cylinder near the free surface. Moreover, if we compare the result for $Re = 200$ and the largest depth $h/D = 1.6$ to the single fluid case 4, we observe that the drag result is barely increased. When the parameter h/D is lower and the structure is closer to the free surface, the drag force coefficients do not match due to the free surface influence.

5.2.2. Effect of Cauchy number

The range of Cauchy numbers studied here is the same as in Section 5.1, with the main results presented in Fig. 24. The reference case 4, with uniform inflow velocity $U/\overline{U} = 1$ and FSI3 properties (Table 3), has been included again for comparison. Focusing on the free surface cases, as all curves for constant Cauchy numbers tend to merge, the dependence on the Cauchy number barely affects the averaged drag. Consequently, the strong dependence of oscillation amplitude

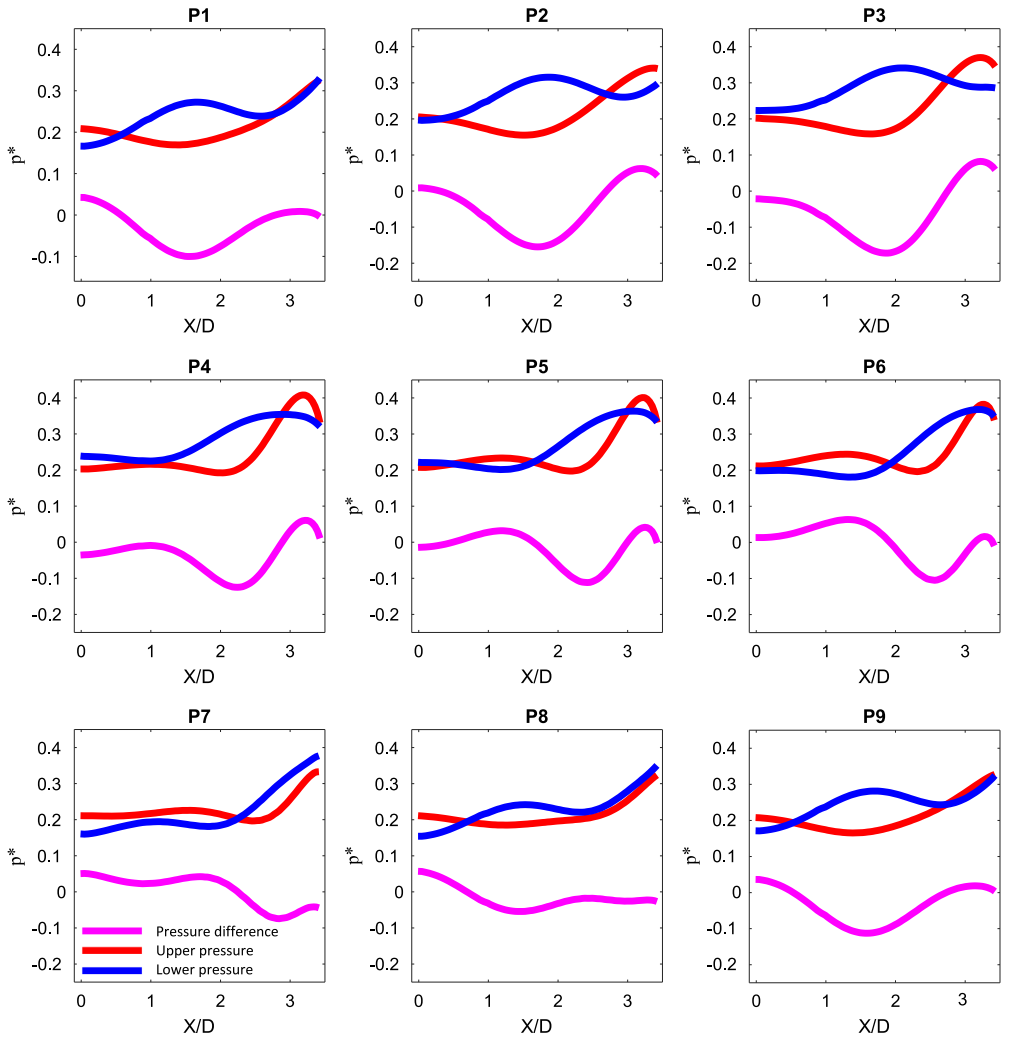

Fig. 19. Normalized pressure values along the top, bottom of the structure and normalized pressure difference at the snapshot.

which clearly increases when the Cauchy number is reduced, see Fig. 20, is not followed by the averaged drag force. In the figure it is obvious how drag values increase linearly with depth independently of the bending stiffness of the plate. This is an indication of the drag term being dominated by the cylinder instead of by the dynamics of the plate. As in the previous results with the *Re*, the time averaged drag forces tend to the value obtained in reference case 4, as the depth is increased.

5.2.3. Effect of Froude number

Here, we analyse how the drag forces vary with depth and with Froude numbers, keeping constant $Re = 200$ and $Cy = 7.14 \cdot 10^{-4}$. Results appear in Fig. 25, where a small dependence of the drag force on the Froude number is depicted. Curves corresponding to the different Froude numbers are close to each other, especially at large depths. The dashed line represents case 4, with uniform inflow velocity $U/\overline{U} = 1$ and FSI3 properties (Table 3), has been included for comparison. Drag increases almost linearly with depth for all Froude numbers. Although the Froude number range is very different to that in Bouscasse et al. (2017), the results presented here for $(Re, Fr, h/D) = (200, 2, 0.6)$, are comparable as they showed a value of 0.92 with $(Re, Fr, h/D) = (180, 2, 0.55)$. Again, only at the largest depths, with a mild effect of the free surface, results tend to the ones obtained in reference case 4.

5.3. Transverse force frequency in the presence of the free surface

In order to evaluate whether the excitation frequencies associated to the transverse force component are close to the natural frequencies of the splitter plate, they have been computed analytically and expressed in dimensionless form using

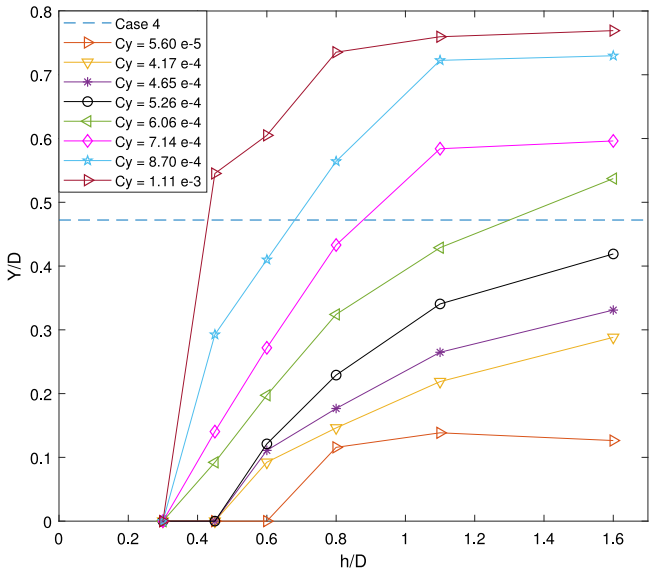

Fig. 20. Splitter plate oscillation versus depth for different Cauchy numbers. The Froude and Reynolds numbers are constant with values: $Fr = 2$ and $Re = 200$. Case 4, with uniform inflow velocity $U/\overline{U} = 1$ and FSI3 properties (Table 3), has been included for comparison in a dashed blue line.

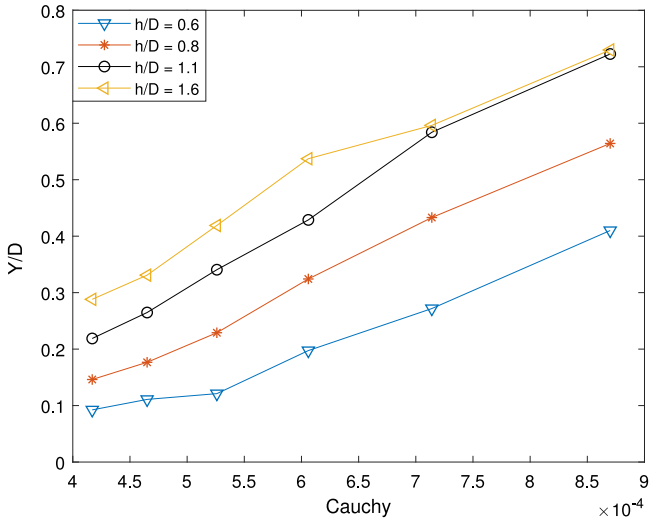

Fig. 21. Comparison between the numerical simulations by changing the Cauchy number and keeping the Froude $Fr = 2$ and the Reynolds $Re = 200$ numbers constant.

the term $D/\overline{U}$. We assume the natural frequencies of the splitter plate can be computed using a model for a cantilevered beam, as given by equation (Kundu et al., 2017).

$$f^*_{n_i} = \frac{D}{\overline{U}} \frac{k_i^2}{2\pi} \sqrt{\frac{EI}{\rho_s A l^4}} \tag{14}$$

where EI is the chord-wise flexural stiffness and A is the cross-sectional area. ρ_s is used for the material density and k_i is a constant that is dependent on the mode number i, and for the first three modes has values of 1.875, 4.694 and 7.855. In the equation, ρ_s includes the added mass. The natural frequencies of the first three modes of vibration, estimated using the above equation, appear in Table 6.

Fig. 26 shows the dominant frequencies of the lift force f_y (after Fourier analysis of the transverse force signal), in dimensionless form ($f^*_y = f_y D/\overline{U}$), for the different cases studied as a function of Re and h/D. In Figs. 27 and 28, the variation of frequencies can be seen as a function of Cauchy and Froude numbers respectively, for the different depths evaluated. In the plots, the dashed lines are used to indicate the natural frequencies ($f^*_{n_i}$) computed using Eq. (14).

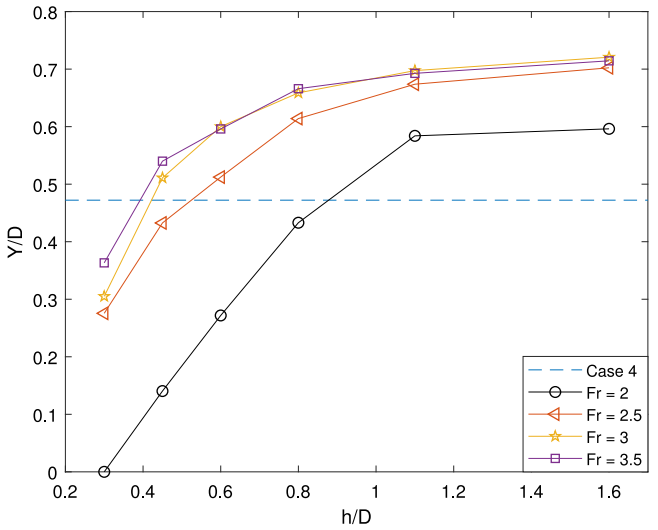

Fig. 22. Vertical oscillation amplitude of point A by changing the Froude number and keeping constant the Cauchy number $Cy = 7.14 \cdot 10^{-4}$ and the Reynolds number $Re = 200$. Case 4, with uniform inflow velocity $U/\overline{U} = 1$ and FSI3 properties (Table 3), has been included for comparison in a dashed blue line.

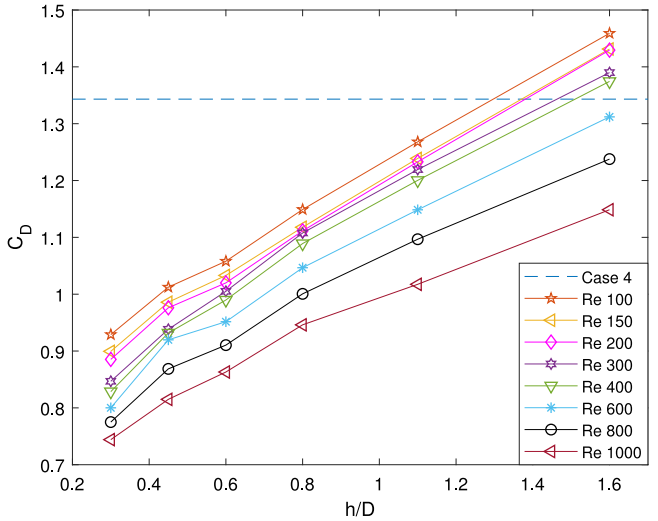

Fig. 23. Drag force versus depth for different Reynolds numbers while keeping constant the Froude $Fr = 2$ and Cauchy numbers $Cy = 7.14 \cdot 10^{-4}$. Case 4, with uniform inflow velocity $U/\overline{U} = 1$ and FSI3 properties (Table 3), has been included for comparison in a dashed blue line.

Table 6
Natural frequencies numbers computed analytically for the different Cauchy numbers taking into account the added mass term.

Cy	$f^*_{n_1}$	$f^*_{n_2}$	$f^*_{n_3}$
1.11e−3	0.11	0.070	0.196
8.70e−4	0.013	0.079	0.222
7.14e−4	0.014	0.087	0.245
6.06e−4	0.015	0.094	0.266
5.26e−4	0.016	0.102	0.285
4.65e−4	0.017	0.108	0.303
4.17e−4	0.018	0.114	0.321
7.15e−5	0.044	0.277	0.774

Fig. 26 depicts a situation in which with the exception of the cases with the lowest Re and when close to the free surface, all runs had monotonically increasing frequencies around 0.2. The same happens in Fig. 27, but in this case for

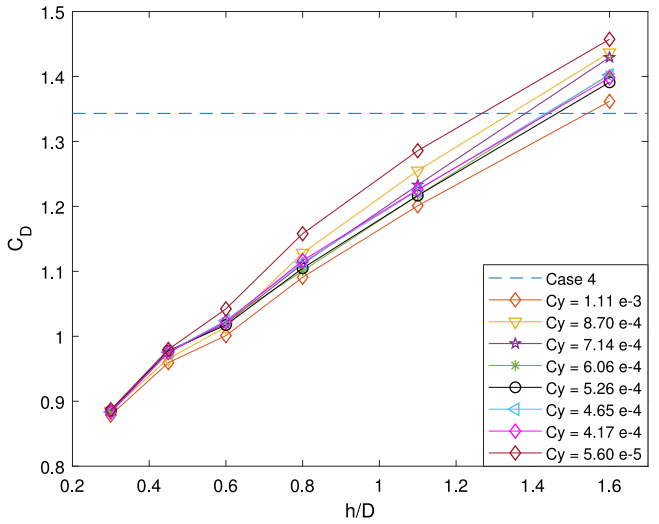

Fig. 24. Averaged drag coefficients C_D changing the Cauchy number and keeping constant the Froude $Fr = 2$ and the Reynolds $Re = 200$ numbers. Case 4, with uniform inflow velocity $U/\overline{U} = 1$ and FSI3 properties (Table 3), has been included for comparison in a dashed blue line.

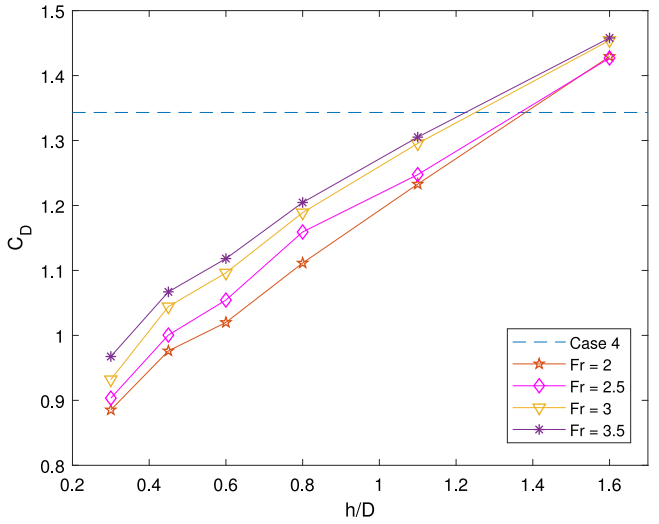

Fig. 25. Averaged drag coefficient versus depth for different Froude numbers, while keeping constant the Cauchy $Cy = 7.14 \cdot 10^{-4}$ and the Reynolds $Re = 200$ numbers. Case 4, with uniform inflow velocity $U/\overline{U} = 1$ and FSI3 properties (Table 3), has been included for comparison in a dashed blue line.

the highest Cauchy numbers. Moreover, the effect of Froude number is very limited as can be seen in Fig. 28. The results indicate how the phenomena is not based on resonance, as natural frequencies are away from the responding frequencies and therefore oscillations are caused by the flow field fluctuations around the splitter plate. The trends imposed by the varying depth yield a different behaviour if compared to that in the results by Zhang and Shi (2016), Rao et al. (2013) and Huang and Sung (2007) in which a fixed solid wall instead of a free surface acted as the near boundary, in studies conducted with rigid plates. In contrast to the rigid plate results presented by Zhang and Shi (2016), here there is no abrupt decrease of frequency for Reynolds numbers higher than 300, and the behaviour found for all Reynolds numbers is very similar.

6. Conclusions

A two dimensional analysis of the dynamics of a flexible splitter plate attached to the base of a cylinder, in laminar regime has been carried out, using numerical techniques. The study is focused on the understanding of the effects of the free surface and the gravity field on the dynamic response and excitation of the elastic splitter plate. The numerical domain is divided by the free surface in two regions with different immiscible fluids. The structure consists of a stationary

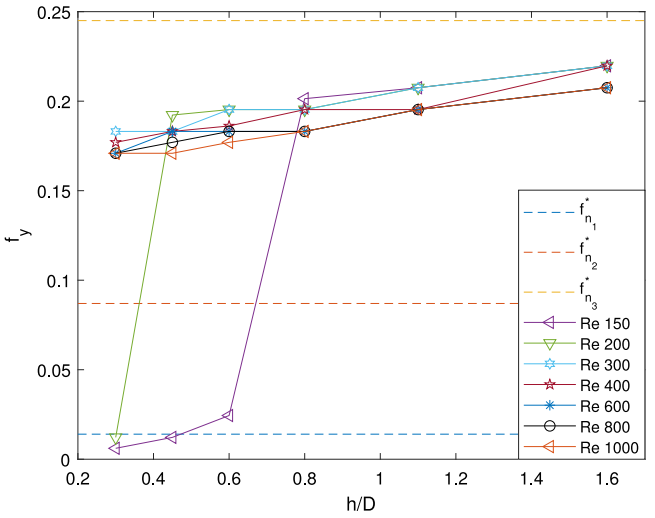

Fig. 26. Frequencies versus depth for different Reynolds numbers, while keeping constant the Froude $Fr = 2$ and the Cauchy $Cy = 7.14 \cdot 10^{-4}$ numbers.

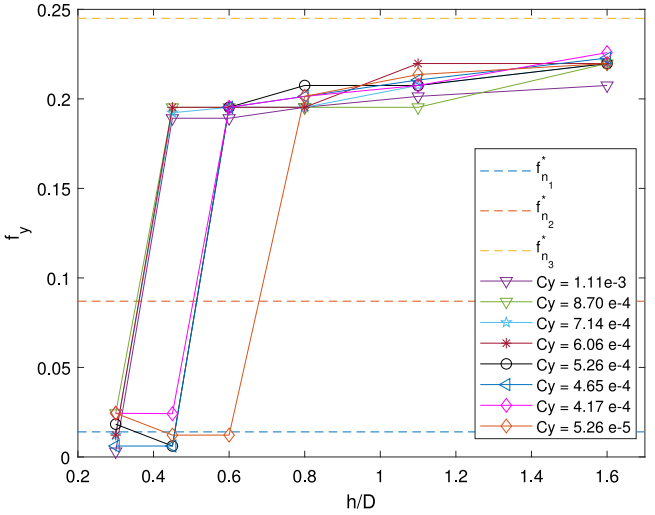

Fig. 27. Frequencies versus depth for different Cauchy numbers, while keeping constant the Froude $Fr = 2$ and the Reynolds $Re = 200$ numbers.

rigid cylinder that has an elastic splitter attached to its base. The work is inspired by the benchmark case posed by Turek et al. (2010), but adding the free surface effects. Reynolds, Froude and Cauchy numbers are systematically varied together with the distance from the structure to the free surface, covering a large parametric space.

Results show how the response of the splitter plate grows monotonically with increasing depth up to a saturated condition in which the free surface does not play a role any more. Moreover, the amplitude of the tip of the splitter plate increases with the Reynolds, Froude and Cauchy numbers as well. The free surface acts as a damping source for the plate dynamics reducing its oscillations. The wave that appears on top of the structure moves forward the separation point of the boundary layer in the upper surface of the cylinder, generating an asymmetry in the shear layers as they detach from the cylinder, yielding a pressure difference that results in decreased splitter oscillations. Within our parameter range, the splitter plate deflects with a shape that is based on either a first mode of vibration or a combination of the first and the second modes. The dominant frequencies of the oscillations are far from the natural frequencies estimated for the splitter plate, suggesting non resonant conditions. The drag coefficient increases linearly with depth, and decreases as expected when the viscosity of the fluid is reduced, without presenting a relevant dependence on the Cauchy and Froude numbers.

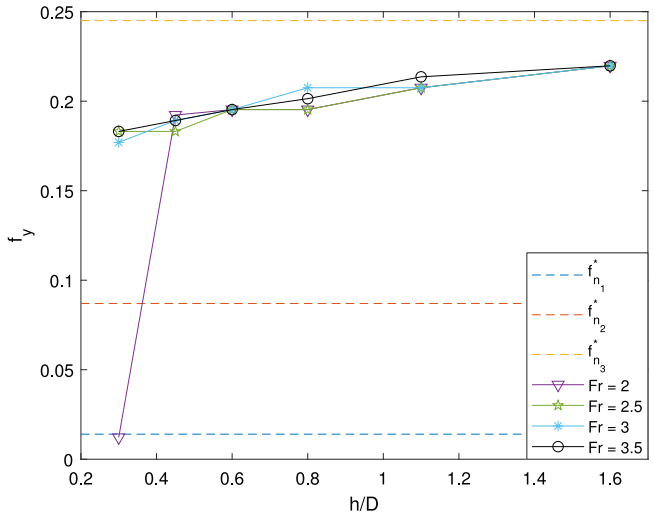

Fig. 28. Frequencies versus depth for different Froude numbers, while keeping constant the Cauchy $Cy = 7.14 \cdot 10^{-4}$ and the Reynolds $Re = 200$ numbers.

Acknowledgements

H.R. Díaz-Ojeda acknowledges the funding provided by Fundación Marqués de Suanzes, ETSIN (UPM). F.J. Huera-Huarte acknowledges the funding provided by the Spanish Ministerio de Economía y Competitividad through grant DPI2015-71645-P is gratefully acknowledged.

References

Allen, J.J., Smits, A.J., 2001. Energy harvesting EEL. J. Fluids Struct. 15, 629–640.
Assi, G., Bearman, P., Kitney, N., 2009. Low drag solutions for suppressing vortex-induced vibration of circular cylinders. J. Fluids Struct. 25 (4), 666–675, bluff Body Wakes and Vortex-Induced Vibrations (BBVIV-5).
Bhardwaj, R., Mittal, R., 2012. Benchmarking a coupled immersed boundary finite element solver for large scale flow induced deformation. AIAA 50 (7).
Bouscasse, B., Colagrossi, A., Marrone, S., Souto-Iglesias, A., 2017. SPH modelling of viscous flow past a circular cylinder interacting with a free surface. Comput. & Fluids 146, 190–212.
Degroote, J., Bathe, K.-J., Vierendeels, J., 2009. Performance of a new partitioned procedure versus a monolithic procedure in fluid–structure interaction. Comput. Struct. 87 (11), 793–801, fifth MIT Conference on Computational Fluid and Solid Mechanics. URL: http://www.sciencedirect.com/science/article/pii/S0045794908002605.
Dimas, A.A., Triantafyllou, G.S., 1994. Nonlinear interaction of shear flow with a free surface. J. Fluid Mech. 260, 211–246.
Gallegos, R., Sharma, R., 2016. Dynamic behaviour of a flexible plate behind a circular cylinder: Numerical study on the effects of blockage and cylinder size. In: 20th Australasian Fluid Mechanics Conference, Perth, Australia.
Huang, W., Sung, H., 2007. Vortex shedding from a circular cylinder near a moving wall. J. Fluids Struct. 23 (7), 1064–1076.
Huera-Huarte, F., 2014. On splitter plate coverage for suppression of vortex-induced vibrations of flexible cylinders. Appl. Ocean Res. 48, 244–249.
Kundu, A., Soti, A.K., Bhardwaj, R., Thompson, M.C., 2017. The response of an elastic splitter plate attached to a cylinder to laminar pulsatile flow. J. Fluids Struct. 68, 423–443, URL: http://www.sciencedirect.com/science/article/pii/S0889974615302115.
Lee, J., You, D., 2013. Study of vortex-shedding-induced vibration of a flexible splitter plate behind a cylinder. Phys. Fluids 25.
Lou, M., Chen, Z., Chen, P., 2016. Experimental investigation of the suppression of vortex induced vibration of two interfering risers with splitter plates. J. Nat. Gas Sci. Eng. 35, 736–752, URL: http://www.sciencedirect.com/science/article/pii/S1875510016306527.
OpenFOAM, 2018. https://sourceforge.net/projects/openfoam-extend/. OpenFOAM Extend.
Oro, J.M.F., 2012. Técnicas numéricas en ingeniería de fluidos. In: Introducción a La Dinámica De Fluidos Computacional (CFD) Por El Método De Volúmenes Finitos. Reverté.
Pisacreta, C., 2017. Fluid Stucture Interactions Flows. Ph.D. Thesis. Salerno University.
Rao, A., Thompson, M., Leweke, T., Hourigan, K., 2013. The flow past a circular cylinder translating at different heights above a wall. J. Fluids Struct. 41, 9–21.
Reichl, P., Hourigan, K., Thompson, M.C., 2005. Flow past a cylinder close to a free surface. J. Fluid Mech. 533, 269–296.
Shukla, S., Govardhan, R., Arakeri, J., 2013. Dynamics of a flexible splitter plate in the wake of a circular cylinder. J. Fluids Struct. 41, 127–134.
Taylor, G., Burns, J.R., Kammann, S.M., Powers, W.B., R. Welsh, T., 2001. The energy harvesting EEL: A small subsurface ocean/river power generator. IEEE J. Ocean. Eng. 26, 539–547.
Triantafyllou, G.S., Dimas, A.A., 1989. Interaction of two-dimensional separated flows with a free surface at low froude numbers. Phys. Fluids A 1 (11), 1813–1821, URL: https://doi.org/10.1063/1.857507.
Turek, S., Hron, J., 2007. Proposal for numerical benchmarking of fluid–structure interaction between an elastic object and laminar incompressible flow.
Turek, S., Hron, J., Razzaq, M., Wobker, H., Schäfer, M., 2010. Numerical Benchmarking of Fluid-Structure Interaction: A Comparison of Different Discretization and Solution Approaches. Springer Berlin Heidelberg, Berlin, Heidelberg, pp. 413–424. http://dx.doi.org/10.1007/978-3-642-14206-2_15.
Versteeg, H.K., Malalasekera, W., 2007. An introduction to computational fluid dynamics. In: The Finite Volume Method. Pearson Education Ltd..
Zhang, H., Shi, W., 2016. Numerical simulation of flow over a circular cylinder with a splitter plate near a moving wall. Ocean Eng. 122, 162–171.